Journal of
Materials Chemistry C

PAPER

View Article Online
View Journal | View Issue

Cite this: *J. Mater. Chem. C*, 2021, **9**, 16257

New thiophene-based conjugated macrocycles for optoelectronic applications†

John Marques dos Santos,[a] Lethy Krishnan Jagadamma,[b] Joseph Cameron,[a] Alan A. Wiles,[a] Claire Wilson,[a] Peter J. Skabara,*[a] Ifor D. W. Samuel*[b] and Graeme Cooke*[a]

Received 30th April 2021,
Accepted 24th June 2021

DOI: 10.1039/d1tc02002a

rsc.li/materials-c

Thiophene-based semiconductors are amongst the most successful materials in organic electronics. In this contribution, we present the synthesis and characterisation of two thiophene-based macrocycles as well as their evaluation in organic-electronic devices. **McT-1** is composed of ten thiophene moieties, whereas in **McT-2**, four additional electron-deficient benzothiadiazole moieties are incorporated to form a donor–acceptor (D–A) π-system. Red-shifted and broadened absorption spectra as well as more positive redox potentials are observed in **McT-2**, whereas **McT-1** displays a sharper absorption band with a higher extinction coefficient. Macrocycle **McT-1** shows emission in the yellow region whereas **McT-2** displays emission in the red wavelength region. DFT calculations predict the macrocycles to comprise of mainly the *E*,*E* isomers with a near-planar structure, which is further supported by the single crystal X-ray structure for **McT-1**. Their charge transporting properties are determined by fabricating thin-film OFETs. The photovoltaic properties of **McT-1** and **McT-2** are also investigated by fabricating bulk heterojunction (BHJ) devices and their potential as photodetectors has been evaluated.

Introduction

Small molecules and polymers used as active components of organic electronics have received a very high level of attention in recent decades owing to their wide range of attractive features including solution processability, tunable absorption and energy levels, high carrier mobility, and photochemical and thermal stability.[1–9] Several devices have evolved through the use of these materials, such as field-effect transistors (FETs) for microelectronics,[10,11] light-emitting diodes (LEDs) for lighting and displays,[12–15] sensors,[16–18] lasers,[19–21] molecular switches[22–24] and photovoltaics.[25–31] Despite the tremendous achievements in recent years that have led to the commercialisation of these devices, significant efforts are still devoted to enhance their performance, improve their processability and stability and understand their functionality. Hence, it is of great interest to investigate different or novel molecular systems to allow the discovery of crucial structure–activity relationships that will allow the development of newer materials with enhanced processability and performance.[32–37]

In both polymer and small molecule based bulk-heterojunction (BHJ) organic photovoltaics (OPVs), the self-assembly of photoactive materials is crucial to generate efficient devices.[38,39] Efficient interaction between donor and acceptor materials is needed to facilitate charge separation,[40] and appropriate intermolecular organisation favours charge transport.[41] Fibre-like domains of active materials with desirable phase-separation or nanowires are often described as efficient morphologies for BHJ OPVs.[36,42] Molecular organisation and orientation are also important for other technologies such as organic light-emitting diodes (OLEDs)[43,44] and organic field-effect transistors (OFETs).[45–49] However, despite being an important and effective concept, the control of the construction of such assembles is challenging.[50,51] In this regard, molecular recognition is promising to manipulate molecular organisation for effective self-assembly of photoactive materials.[52]

Conjugated macrocycles appear in this scenario as an emerging family of materials with great potential for optoelectronic applications.[53–56] These materials possess unique features including their controlled structure that can facilitate intermolecular arrangement,[57] and their defined cavity that can be used to host electronically active molecules such as fullerene derivatives.[58,59] Furthermore, by virtue of their cyclic structure, they do not feature end-group functionalisation, which often result in charge traps in linear molecules.[53] In addition, their

---

[a] School of Chemistry, University of Glasgow, Glasgow, G12 8QQ, UK. E-mail: graeme.cooke@glasgow.ac.uk, peter.skabara@glasgow.ac.uk

[b] Organic Semiconductor Centre, SUPA, School of Physics and Astronomy, University of St. Andrews, St. Andrews, Fife, KY16 9SS, UK. E-mail: idws@st-andrews.ac.uk

† Electronic supplementary information (ESI) available: Synthesis of macrocycles and the additional characterisation data highlighted in the manuscript. CCDC 2063123. For ESI and crystallographic data in CIF or other electronic format see DOI: 10.1039/d1tc02002a

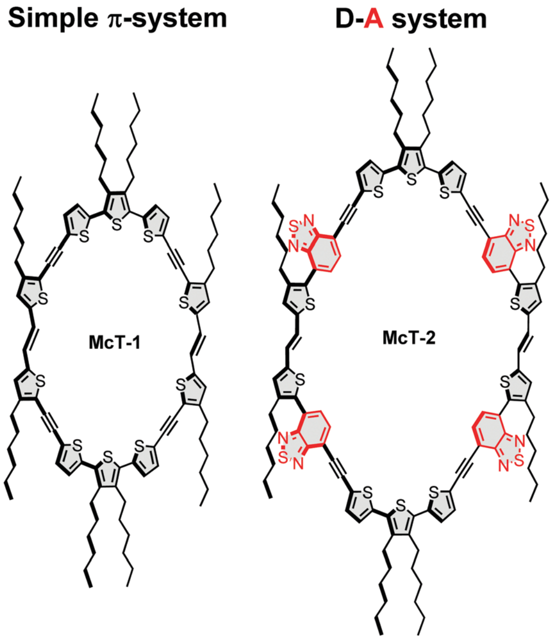

Fig. 1 Scheme showing the thiophene-based macrocycles synthesised and investigated in this study.

extended conjugation with highly aligned molecular frontier orbitals often leads to desirable electronic properties such as high intramolecular charge transfer (ICT).[60–62] These positive features can be exploited to deliver optimum morphologies in optoelectronic devices and pave the way to more efficient charge transfer/transport.

A great number of reports have made available protocols for the synthesis of macrocycles composed of a wide variety of aromatic moieties such as: benzene, carbazole, thiophene, perylene, porphyrin, BODIPY, furan, acetylene and so forth.[35,54,56,63–73] Previous work reports the synthesis of cycles of different molecular lengths and cavity sizes.[74,75] Some also report the formation of stable supramolecular complexes with different substrates.[76–81] However, in spite of such interesting discoveries, examples of direct application of these interesting molecules in optoelectronic devices are still limited.[58,60,82–90] Some of the pioneering reports include, for instance, a triphenylamine-based compound (namely **3B2A**) reported by Zhang *et al.*,[86] and a perylene diimide (PDI)-based compound (namely **cPBPB**) reported by Ball *et al.* (see Fig. S1 in ESI†).[55,58] The former was applied as a donor material in a BHJ device showing a power conversion efficiency (PCE) of 2.66% in a blend with a fullerene derivative (**PC$_{71}$BM**), whereas the latter was built to mimic fullerenes and take advantage of their useful properties such as three dimensional shape and fully delocalised π-space with a low lying LUMO. Interestingly, the BHJ cell incorporating **cPBPB** as the acceptor (with **PTB7-Th** as the donor) reached a PCE of 3.5% that outperformed an unfolded oligomer and a polymer of the same kind. These recent results emphasise the potential of conjugated macrocycles for optoelectronic applications.

In this contribution, we report two new thiophene-based conjugated macrocycles. Compound **McT-1** possesses a conjugated π-system composed of only thiophene units, whereas the formation of a donor–acceptor (D–A) system is explored in compound **McT-2** with the insertion of two benzothiadiazole (BT) moieties in each semicircular unit (Fig. 1). Thiophene moieties are found in many of the high efficiency small molecule and polymer-based OPVs[27,91–96] and OFET materials,[10,11,46] due to their excellent charge transport, high stability and polarisability, fluorescence properties and ability to form highly electron-conductive composites. Also, in comparison with benzene, thiophene shows weaker aromaticity and lower steric hindrance between neighbouring units; which leads to smaller band-gaps due to increased quinoidal character upon π-electron delocalisation and improved planarity.[25,75,97–101] Therefore, it is of great importance to investigate macrocyclic systems of this kind. Utilising the well-established McMurry reaction, alkyne-spaced building blocks were used in order to suppress steric hindrance and facilitate the cyclisation step, as is common when constructing such molecular systems.[57,74] However, considering results discussed in our previous report which pointed that alkyne spacers are detrimental to charge transfer, charge generation and ultimate photovoltaic performance in thiophene-based molecules,[102] the macrocycles were designed to minimise the number of alkyne groups compared to other reported systems, with only four present in each macrocycle. The synthesis of the new macrocycles was accomplished *via* dimerisation of two oligothiophene units, in which the concentration of the reacting species was key to yield the desired products. The UV-vis absorption and emission profiles are compared, while DFT calculations are used to investigate the nature of the electronic transitions and probe both their frontier molecular orbitals and molecular conformation. A single crystal X-ray structure was obtained for **McT-1**, from which it was possible to confirm its molecular structure and arrangement. Their potential as semiconductors is unlocked by fabricating bottom-contact OFETs and BHJ photovoltaic devices (with the macrocycles as the donor and **PC$_{71}$BM** as the acceptor). Their relatively narrow spectral bandwidth allowed us to investigate their use in photodetectors without using filters in colour image sensing.

Results and discussion

Synthesis and molecular design

The synthetic pathway for the target molecules involved the use of Sonogashira reactions to produce the oligothiophene building blocks (see ESI†) and a McMurry coupling for the cyclisation steps (see Scheme 1). The Sonogashira cross-coupling reaction has been used extensively in the construction of these systems, providing the appropriate spacing of adjacent thiophene moieties and suppressing twisted dihedral angles.[103,104] However, in this work the number of alkynes were minimised, contrasting with the most common thiophene-based macrocycles reported.[57,71,74] This leads to a challenging molecular arrangement of the parallel thiophenes since they usually tend to arrange in an *anti*-conformation when in a linear system.[92,101]

In order to achieve an optimal yield by facilitating the cyclisation and suppressing polymerisation, the total concentration of

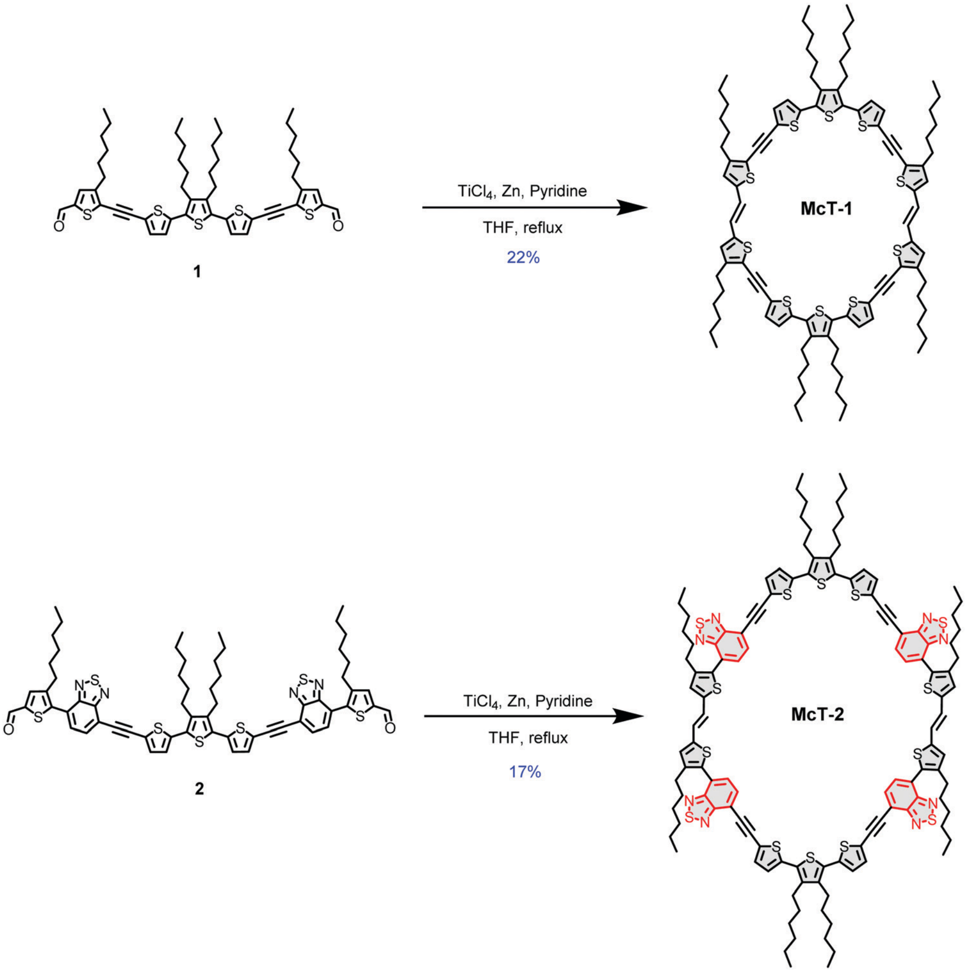

Scheme 1 Synthesis of compounds **McT-1** and **McT-2**.

the reacting species (compounds **1** and **2**) was optimised as summarised in Tables S1 and S2 (provided in the ESI†). For **McT-1**, the yield improved significantly on going from a 1.8 mM (2%) to a 3.6 mM (22%) concentration of compound **1**. For **McT-2**, only 7% yield was achieved using a 1.0 mM concentration of compound **2**, while at a 1.3 mM concentration the yield improved to 17%. In both cases, further increasing the concentration of the starting material decreased the yield considerably, possibly due to polymerisation now being more favoured.

Thermal properties

The thermal properties of **McT-1** and **McT-2** were studied using thermogravimetric analysis (TGA) and differential scanning calorimetry (DSC). TGA was studied to compare the thermal stability of the two macrocycles with the plots shown in Fig. S12 (ESI†). The temperature of 5% mass loss for **McT-1** was 401 °C, showing that this macrocycle has good thermal stability. However **McT-2** showed a much-reduced temperature of 5% mass loss at 228 °C and suggests that the increased strain caused by increasing the size of the macrocycle leads to a reduction in its thermal stability.

DSC plots are shown in Fig. S13 (ESI†). The heating and cooling scans for **McT-1** show no obvious phase transitions between 25 °C and 300 °C, which is an advantage for device processing as the material can be annealed without crystallisation and subsequent formation of grain boundaries. On heating **McT-2**, there is a melt peak at 50.1 °C and in the reverse scan the peak at 45.5 °C indicates crystallisation upon cooling. This phase change at relatively low temperature may be detrimental to device performance.

Optical and electrochemical properties

The absorption spectra of both macrocycles (5×10^{-6} M in CH_2Cl_2) are shown in Fig. 2. **McT-1** showed a weak absorbance band in a shorter wavelength region, *ca.* 300 nm, and a sharp, strong absorbance band at 438 nm (maximum absorbance, λ_{max}) (Fig. 2(a)). **McT-2**, however, presented two strong absorbance peaks at shorter wavelengths (*ca.* 325 nm and 375 nm) and a λ_{max} at 476 nm (Fig. 2(b)). The bands at maximum absorbance are often a result of S_0–S_1 and S_0–S_2 type transitions.[72] Notably, this band red-shifts for the BT-containing macrocycle **McT-2** (*ca.* 30 nm) with respect to **McT-1**, with the former also showing a broader spectrum and a high absorbance throughout most of the region covered. This phenomenon is ascribed to a pronounced ICT effect since the electron-withdrawing BT moieties induce a push–pull effect in this D–A system. Furthermore, new bands observed at around 320–400 nm are likely originating from the BT unit's

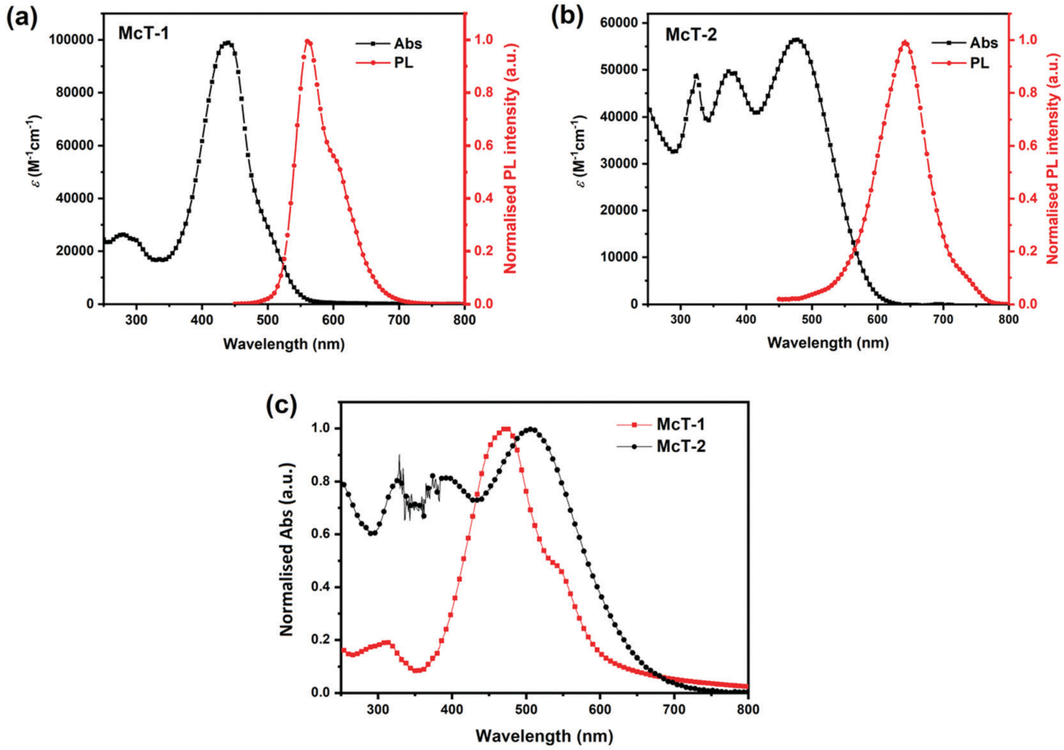

Fig. 2 Absorption and fluorescence spectra of **McT-1** (a) and **McT-2** (b) in solution state (CH_2Cl_2, 5×10^{-6} M) (the fluorescence spectra were excited at 440 and 480 nm for **McT-1** and **McT-2**, respectively). (c) Normalised absorption spectra of **McT-1** and **McT-2** in thin film form.

π–π* internal transition.[105] On the other hand, the simplest macrocyclic compound (**McT-1**) presented a higher value of extinction coefficient (ε_{max}, 98 890 M^{-1} cm^{-1}) than its BT-containing analogue (56 560 M^{-1} cm^{-1}). Values relating to the onset of absorbance (λ_{onset}) were estimated as 561 nm for **McT-1** and 612 nm for **McT-2**, and correspond to optical band-gap (E_{opt}) values of 2.21 eV and 2.02 eV, respectively. In thin films (Fig. 2(c)), the two macrocycles present bathochromic shifts in λ_{max} (*ca.* 30 nm), typically as a result of enhanced π–π stacking interactions. Furthermore, the main absorbance band is broadened and extends to longer wavelength for both compounds, while for **McT-1** the insurgence of a shoulder at *ca.* 545 nm is seen which is perhaps a vibronic level or due to π–π stacking. The optical data are summarised in Table 1.

The emission spectra of the two macrocycles were recorded in solution (Fig. 2(a and b)). **McT-1** shows an emission peak at 560 nm (with a vibronic shoulder around 600 nm) and **McT-2** presents a peak at 642 nm with reasonably sharp full-width at half-maximum (FWHM) (*ca.* 70 nm for **McT-1** and 82 nm for **McT-2**). It is also noteworthy that both compounds have large Stokes shifts despite the circularly locked structure. The Stokes shift was higher for **McT-2** (*ca.* 166 nm) than for **McT-1** (122 nm), possibly due to rotation of the BT units after excitation.[106–108] A larger Stokes shift has also been observed in a BT-containing [10]cycloparaphenylene (**BT[10]CPP**) compared to its parent **[10]CPP**.[109]

To study the possible interactions between the macrocycles and fullerenes, fluorescence titration was performed with **McT-1** and **McT-2** in toluene solution, since fluorescence quenching can be indicative of intermolecular interactions.[110,111] This was done through the addition of aliquots of a solution of $\mathbf{C_{60}}$ in toluene. When analysing the fluorescence intensity upon addition of small amounts of $\mathbf{C_{60}}$ (see Fig. S14, ESI†), one can notice a substantial quenching happening only after a considerable increase of $\mathbf{C_{60}}$ concentration in both cases. In fact, *ca.* 65% of the intensity was only quenched after an addition of *ca.* 300 equivalents of $\mathbf{C_{60}}$ to 1 equivalent of **McT-1** and *ca.* 125 equivalents of $\mathbf{C_{60}}$ to 1 equivalent of **McT-2**. According to these

Table 1 Summary of optical and electrochemical data of **McT-1** and **McT-2**

Dye	$\lambda_{max/abs}$[a] (nm)	ε_{max}[a] (M^{-1} cm^{-1})	λ_{max}[b] (nm)	$\lambda_{max/emi}$[a] (nm)	λ_{onset}[a] (nm)	E_{opt}[c] (eV)	$E_{1/2\ ox}$[d] (V)	$E_{1/2\ red}$[d] (V)	IE[e] (eV)	EA[f] (eV)	E_{fund}[g] (eV)
McT-1	438	98 890	473	560	561	2.21	0.17	−1.88	−5.0	−2.9	2.1
McT-2	476	56 560	502	642	612	2.02	0.03	−1.62	−4.8	−3.2	1.6

[a] Measured in dichloromethane (5×10^{-6} M). [b] Measured in thin film. [c] Calculated using the formula $E_{opt} = 1240/\lambda_{onset}$. [d] Measured by square wave voltammetry in dichloromethane (1×10^{-3} M) and calibrated *versus* the ferrocene/ferrocenium (Fc/Fc^+) redox couple. [e] Calculated using the formula $IE = -[E_{ox} + 4.8]$ eV.[114] [f] Calculated using the formula $EA = -[E_{red} + 4.8\ eV]$.[114] [g] Calculated using the formula $E_{fund} = |IE - EA|$ eV.[114]

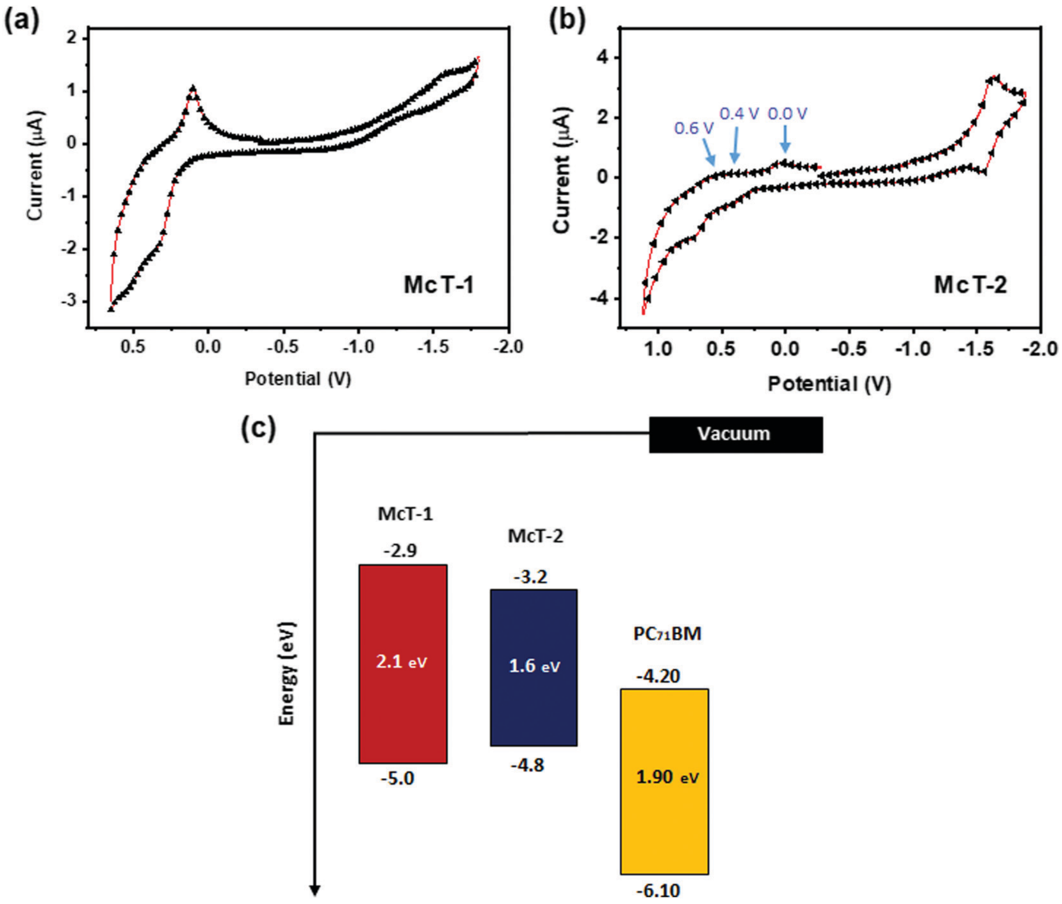

Fig. 3 Cyclic voltammograms of **McT-1** (a) and **McT-2** (b). The voltammograms were recorded in CH_2Cl_2 solution (1×10^{-3} M). The electrodes used were a 1.6 mm diameter platinum working electrode, a platinum wire counter electrode and a silver wire quasi-reference electrode and the electrolyte of choice was $TBA \cdot PF_6$ (0.1 M). Voltammograms were calibrated *versus* the ferrocene/ferrocenium (Fc/Fc^+) redox couple as an external standard. In (c) the energy level diagram of **McT-1**, **McT-2** and the **$PC_{71}BM$** acceptor (obtained from the literature) is provided.[112,113]

results, we hypothesised that limited cavity filling or complexation between the McT series and **C_{60}** took place in these solutions.

Cyclic voltammetry (CV) and square wave voltammetry (SWV) were used to study the electronic properties of the two molecules. The CV measurements revealed one clear oxidation wave with non-reversible character for **McT-1**, whereas for **McT-2**, three low intensity irreversible peaks at *ca.* 0.0 V, 0.4 V and 0.6 V and a quasi-reversible reduction wave was seen [Fig. 3(a and b)]. The SWV measurements revealed in turn a clearer peak of reduction for **McT-1** and two clear reduction peaks for **McT-2** (Fig. S15, ESI†). Utilising the SWV values to estimate the energy levels, the ascribed first reduction peak ($E_{1/2\text{red}}$) of **McT-2** is more positive than for its counterpart, resulting in a lower-lying electron affinity (EA, −3.2 eV) than for **McT-1** (−2.9 eV). The first oxidation peak ($E_{1/2\text{ox}}$) of **McT-1** was found at 0.17 V, resulting in a high-lying ionisation energy (IE) of −5.0 eV. These low values of $E_{1/2\text{ox}}$ and shallow IE are typical of these types of thiophene-based macrocycles.[57,72,76] Surprisingly, a higher IE was observed for electrochemical measurements performed on **McT-2** (−4.8 eV). Hence, based on these data, both **McT-1** and **McT-2** are considered donor type materials, with a fundamental gap (E_{fund}) of 2.1 eV and 1.6 eV, respectively (in accordance with the E_{opt} obtained from solution), and can be used with **PCBMs** as acceptors in BHJ cells (see energy level diagram in Fig. 3(c)).[112,113] The electrochemical data are given in Table 1.

Theoretical calculations

Compounds **McT-1** and **McT-2** were studied using density functional theory (DFT) calculations (B3LYP/6-311G(d,p) level of theory in the gas-phase) to investigate their dihedral angles, conformation and frontier orbital distribution. To gain insight into whether these specific macrocycles would be generated as *E*,*E* or *Z*,*Z* isomers, **McT-2** was first calculated in both forms (*E*,*E* and *Z*,*Z*) and the total energies of both analogues were compared upon geometry optimisation (see Fig. S16 in ESI†). A considerably strained conformation was observed for the *Z*,*Z* isomer of **McT-2**, whereas the *E*,*E* isomer is more planar (Fig. S16, ESI†). For the *E*,*E* isomer, the central thiophene moiety (T1) is allocated *syn* to its two peripheral neighbours (T1 and T10), whereas for the *Z*,Z isomer it is allocated *anti* [see Fig. 4(a) for atom and moiety labels]. A considerably higher bond angle of the vinyl group (bond angle C24–C25–C26 137°) was observed for the *Z*,*Z* isomer of **McT-2** than for *E*,*E* isomer of **McT-2** (126°), which implies that the *Z*,*Z* isomer has a more

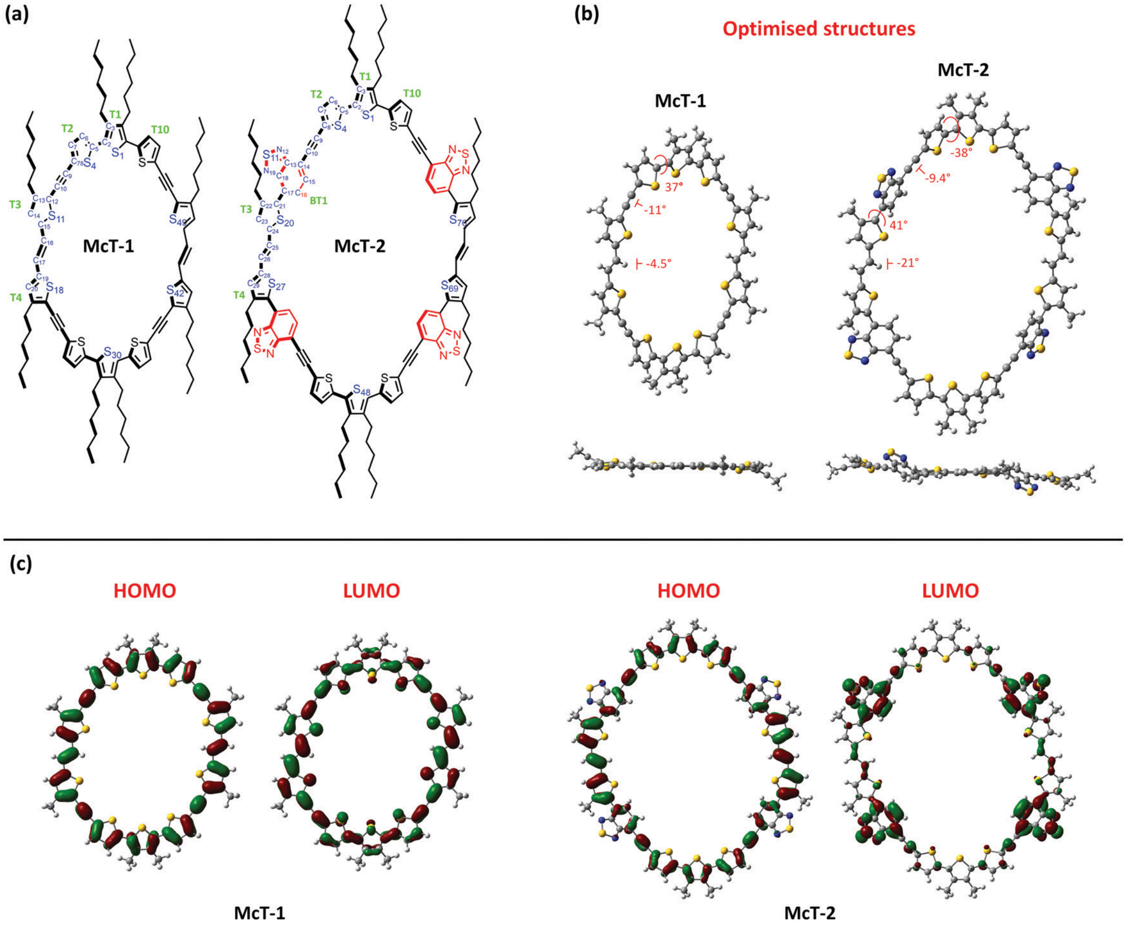

Fig. 4 (a) Illustration of molecular structure of **McT-1** and **McT-2** showing atom labels (T1–10 represents thiophene moieties). (b) Optimised structures from DFT (B3LYP/6-311G(d,p)) of **McT-1** and **McT-2** (diagonal and side views). (c) HOMO and LUMO maps of **McT-1** and **McT-2**.

strained circular structure. A difference of 22 kJ mol^{-1} was found between the *E*,*E* and the *Z*,*Z* isomers ground state total energy, with the *E*,*E*-isomer being the lowest in energy. In the literature, similar compounds with a more regular ratio of alkyne spacers are shown to cyclise in both forms.[76,77] However, due to such strain observed for the *Z*,*Z* isomer, it was expected that both macrocycles are present as mainly their *E*,*E* isomers since the transition state conformation in the final synthetic step is likely to affect the activation energy to form the product. In such forms, both compounds show near-planar structure. For **McT-1** only the central thiophene moiety (T1) shows a moderate dihedral angle with its neighbouring moieties (T2 and T10) (*i.e.* torsion angle S1–C2–C5–S4 36.5°) [Fig. 4(b)], whereas **McT-2** presents a notable dihedral angle of 41.1° also between the moieties T3 and BT1 (C16–C17–C21–S20) due to the alkyl chain.

The ring size is naturally wider/bigger for **McT-2** since it contains 4 more aromatic moieties than **McT-1**. According to the calculations, the cavity size varies between 12.9 Å (S11...S42) to 16.2 Å (S1...S30) for **McT-1** and between 20.1 Å (S20...S69) to 22.8 Å (S1...S48) for **McT-2**. Therefore, it is reasonable to assume that both compounds possess sufficiently large cavities to accommodate guest molecules such as fullerenes. **C_{60}** for instance, has a mean ball diameter of 7.1 Å, whereas **C_{70}** has a short axis of 7.1 Å and a long axis of 7.9 Å.[115] However, due to the absence of alkyne spacers between several thiophene moieties in the macrocycles, both adopt elliptical-like structures. This could potentially discourage fullerene molecules filling the cavity due to steric reasons. This will be especially true for **McT-1**, as the cavity has a considerably shorter axis than the other macrocycle. The frontier orbitals, depicted in Fig. 4(c), are completely delocalised in the case of **McT-1** with a total overlap of HOMO and LUMO. The distribution is different for **McT-2**, where the HOMO appears delocalised along the whole molecule but the LUMO is mostly confined over the BT moieties. This is mainly due to the push–pull system generated with the introduction of the BT moieties, which also causes the red-shift in the UV-vis spectrum. The calculated HOMO (−4.83 eV for **McT-1** and −5.09 eV for **McT-2**) and the LUMO (−2.57 eV for **McT-1** and −3.01 eV for **McT-2**) energy levels (Fig. S17, ESI†) are in good agreement with the IE and EA values obtained experimentally for **McT-1**, whereas for **McT-2** the HOMO is lower than the experimentally derived value (see Table S3, ESI†).

Time-dependent DFT calculations were performed to gain more insight into the optical properties of the materials. These were conducted using the same method (B3LYP/6-311G(d,p) in the gas-phase). The calculations provided a reasonable estimation of the absorption spectrum similar to the experimental data presented in Fig. 2 and Table 1 for both **McT-1** and **McT-2** (Fig. S18, ESI†). Upon analysing the electronic transitions responsible for the main bands of absorption observed for the two molecules (Tables S4 and S5, ESI†), we observed that in both cases the highest wavelength absorbance bands (around 500 nm for **McT-1** and 630 nm for **McT-2**) are composed of four excited states (S_2, S_3, S_4 and S_6 for **McT-1**, and S_2, S_3, S_4 and S_7 for **McT-2**). This band is dominated by a transition from the HOMO−1 to the LUMO ($S_0 \rightarrow S_3$) for **McT-1** and from the HOMO to the LUMO+1 ($S_0 \rightarrow S_2$) for **McT-2**, the latter being ICT in nature. The lower wavelength absorbance (*ca.* 370 nm for **McT-1** and *ca.* 440 for **McT-2**) splits between two main excited states (S_{16} and S_{17} for **McT-1**, and S_{21} and S_{23} for **McT-2**), resulting from a strong contribution of HOMO−1 to LUMO+4 for **McT-1** and HOMO to LUMO+6 for **McT-2**. Plots of selected molecular orbital density maps is provided in Fig. S19 (ESI†) for **McT-1** and Fig. S20 (ESI†) for **McT-2**, including those involved in the strongest transitions described here. These orbitals are also delocalised mostly along the whole molecule for **McT-1**, whereas for **McT-2** the LUMO+6 is also delocalised over the thiophenes T3, T4, T8 and T9 and the vinyl residues.

X-Ray structures

Single crystals of **McT-1** were obtained from slow diffusion of heptane in a benzene solution, and its structure was determined by X-ray analysis. Unfortunately, attempts to obtain single crystals of **McT-2** were unsuccessful. The X-ray crystal structure of **McT-1** (Fig. 5(a)) shows all the thiophene sulfur atoms face into the centre of the macrocycle and is consistent with the calculated prediction that the vinyl groups would be *E*-isomers. **McT-1** crystallises with half the molecule in the asymmetric unit and the other half is related by inversion symmetry. The two crystallographically independent alkyne bonds have different conformations, with one having two almost exactly coplanar thiophene rings (angle between mean planes 0.99°) and the other with the two rings tilted at 27.75° to one another. The three linked thiophene rings have two rings essentially coplanar (torsion angles S4–C5–C2–S1 $-2.0(8)^\circ$) and the other two tilted at $\sim 30^\circ$ (torsion angle S25–C29–C30–S1i−31.3(8)°). Apart from this tilted thiophene ring the macrocycle is essentially planar. The alkyl chain substituents on the central S1 thiophene both lie out of the plane on the same side for a given thiophene ring (also the same side for adjacent ring S18) and on the opposite side to the symmetry equivalent S1 thiophene on the other side of the macrocycle. The S1…S1(i) distance is 16.406(2) Å and S18…S11(i) 12.423(2) Å. Examination of the packing in **McT-1** (Fig. 5(b) and Fig. S21, ESI†) shows that the cavities are filled by the alkyl chains from adjacent molecules. Each cavity contains four chains in total with two each from adjacent S1 two pointing downwards and two upwards forming zig-zag chains. These chains are then 'cross-linked' by the S…S contacts between the two S atoms across the other pair of alkyne bonds (S4 and S11) with an adjacent chain at approximately the sum of the van der Waals radii at just under 3.6 Å. The adjacent chain is shown in green in Fig. 5(b).

Organic field-effect transistors

The charge transporting properties of the macrocycles were studied in bottom-gate, bottom-contact OFETs. **McT-1** was deposited in two different solutions, chloroform and toluene, to determine whether this influenced the performance of the OFETs. Devices containing **McT-2** did not show any field-effect in either p-type or n-type transistors. This may be explained by the increased twisting in the macrocycle as a result of introducing the benzothiadiazole unit, as shown by theoretical calculations in Fig. 4b. DSC data also showed that there is a relatively low melt temperature which suggests **McT-2** may undergo a phase change when a voltage is applied across the channel, particularly if there is a high resistance. Moreover, **McT-2**, showed weak oxidation peaks in cyclic and square-wave voltammetry experiments, suggesting that it may be a poor p-type material.

Examples of the OFET characteristics for **McT-1** containing OFETs are shown in Fig. 6 and a summary of the averaged data is presented in Table 2. There are small differences in performance of the OFETs when the solvent is varied. The p-type mobilities are similar at $1.92 \pm 0.8 \times 10^{-4}$ cm^2 V^{-1} s^{-1} when deposited from toluene and $1.66 \pm 0.6 \times 10^{-4}$ cm^2 V^{-1} s^{-1} when chloroform is used. The on/off ratios are relatively low at 10^2 which is mainly caused by the relatively low ON current, due to the limited hole mobility, but also partly due to a higher OFF current due to relatively short channel lengths (5, 10 and 20 μm). The main difference is in the threshold voltage which is slightly reduced for OFETs fabricated using toluene. These differences may be influenced by the slower drying of toluene compared to chloroform.

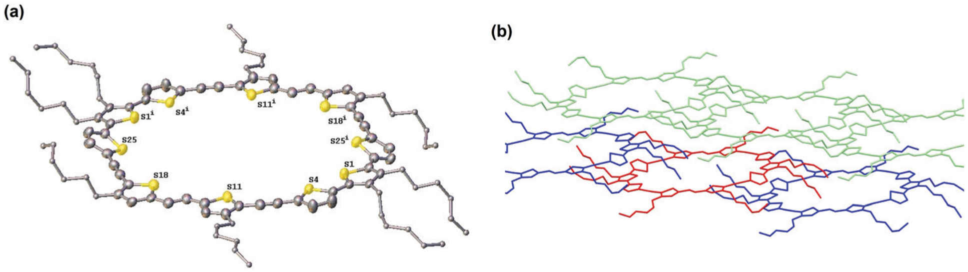

Fig. 5 (a) View showing **McT-1** in the crystal structure (H atoms and minor alkyl chain disorder components omitted for clarity, displacement ellipsoids drawn at 50% probability level while alkyl chains drawn as spheres of arbitrary radius). The two halves of the molecule are related by an inversion centre ($i = 1 - x, -y, -z$). (b) Shows that the cavities are filled by the four alkyl chains, 2 each from adjacent molecules (shown in blue); an adjacent chain is shown in green.

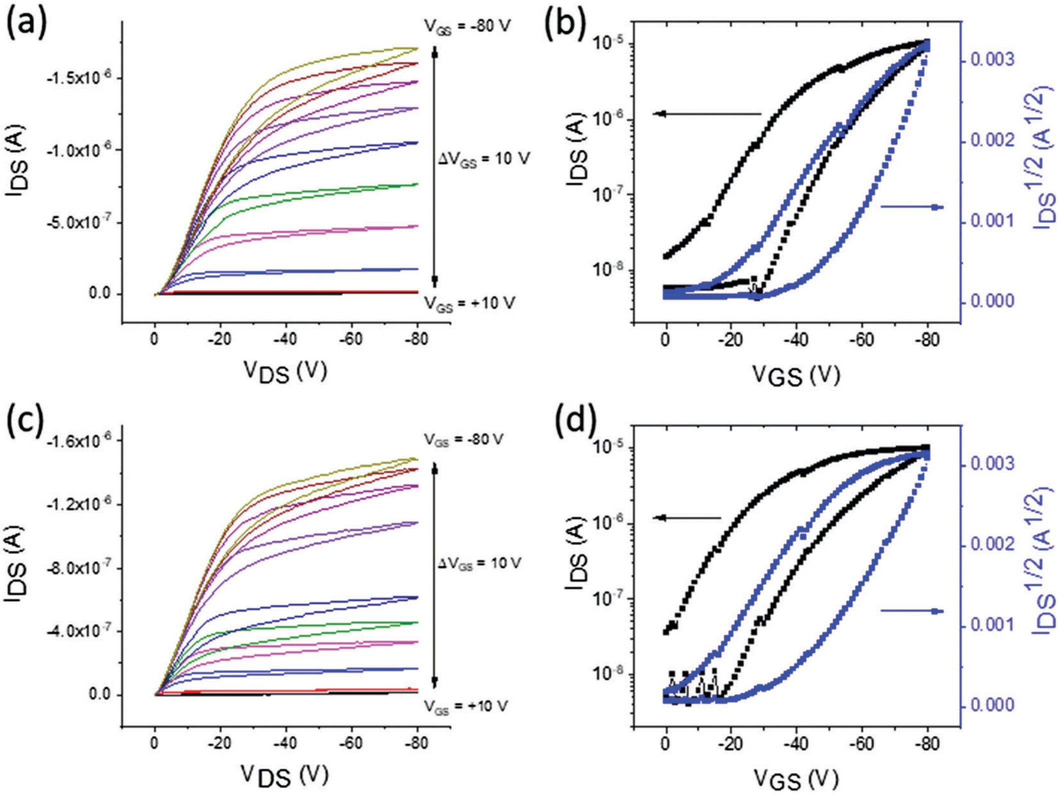

Fig. 6 Characterisation of OFETs fabricated using **McT-1**, channel length = 10 μm, channel width = 1cm. Output characteristics of OFETs fabricated using **McT-1** in (a) chloroform and (c) toluene solutions. Transfer graphs for **McT-1** films deposited using (b) chloroform and (d) toluene solutions where V_{DS} = −70 V.

Table 2 Summary of OFET performance of **McT-1** deposited from chloroform and toluene solutions

Solvent	On/off ratio	V_{th} [V]	μ_h [cm^2 V^{-1} s^{-1}]
Chloroform	10^2	−9	$1.66 \pm 0.6 \times 10^{-4}$
Toluene	10^2	−1	$1.92 \pm 0.8 \times 10^{-4}$

Atomic force microscopy was used to study the difference in the topographies of the films. Images with scan area 10 × 10 μm^2 are presented in Fig. 7 as well at 5 × 5 μm^2 and 20 × 20 μm^2 in Fig. S22 and S23 (ESI†), respectively. The general topographies show similarities, with holes emerging in both films. However, the film deposited from chloroform shows smaller, more isolated domains whilst the films formed from toluene show larger domains although there are still pinholes present. The difference in topographies may result from the lower boiling point of chloroform causing quicker drying of the film. The gaps observed in the morphology of both films could help to explain the low mobilities measured, since charge transport will be limited with so many disconnections in the bulk. However, the closeness of

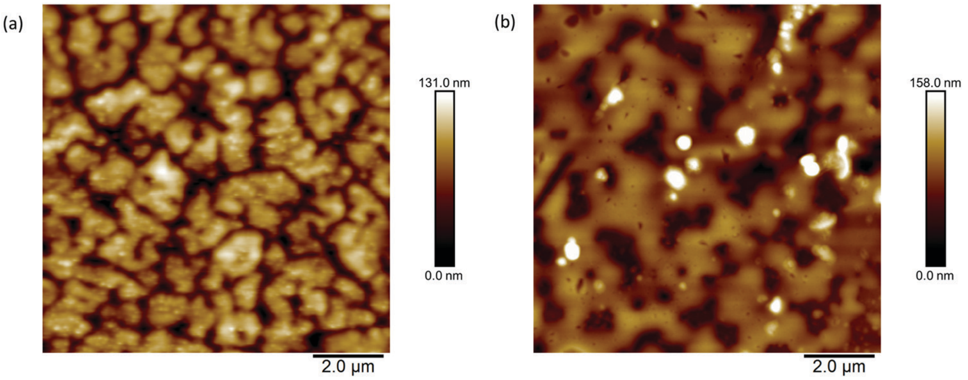

Fig. 7 Tapping mode atomic force microscopy images of **McT-1** films deposited from (a) chloroform (RMS roughness = 17.8 nm) and (b) toluene (RMS roughness = 22.8 nm) solutions on prefabricated OFET substrates. Scan area = 10 × 10 μm^2.

the general topographies is consistent with the similar calculated hole mobilities.

Photovoltaic properties

To investigate the photovoltaic properties of **McT-1** and **McT-2**, bulk heterojunction solar cells were fabricated using **$PC_{71}BM$** as the acceptor. Before proceeding with device fabrication, charge transfer of **McT-1** and **McT-2** donors to the **$PC_{71}BM$** acceptor was investigated using photoluminescence quenching studies. Efficient charge transfer from the donor to acceptor will quench the photoluminescence of the donor molecules. The steady-state luminescence spectra of the neat donor molecules and their blends with **$PC_{71}BM$** for different weight ratios (1 : 1, 1 : 2, 1 : 3 and 1 : 4) are shown in Fig. 8(a and b). With the addition of **$PC_{71}BM$**, for both donor molecules, the photoluminescence is significantly quenched which implies that there is efficient charge transfer from the donors **McT-1** and **McT-2** to the acceptor. The UV-Vis absorption properties of these different blend films are shown in Fig. 8(c and d). For both the blends the absorption bandwidth is narrow and mainly in the region 400–600 nm.

With the efficient charge transfer properties confirmed through the PL quenching, solution-processed organic solar cells were fabricated for both **McT-1** and **McT-2** using different donor : acceptor (**$PC_{71}BM$**) ratios of 1 : 1, 1 : 2, 1 : 3 and 1 : 4. The photovoltaic performance parameters of the corresponding blend films are shown in Table 3 and the *J–V* characteristics are shown in Fig. 9(a and b). For **McT-1** with the increase of **$PC_{71}BM$** content, the power conversion efficiency increases and at the optimised blend ratio of 1 : 4, the corresponding solar cells show an efficiency of ∼1.1%. Photovoltaic devices with higher blend ratios were not fabricated since the power conversion efficiencies for the 1 : 3 and 1 : 4 blends are very similar. For **McT-2:$PC_{71}BM$** blends, a similar trend is seen and the highest efficiency of 0.63% is obtained for 1 : 3 donor : acceptor ratio.

For both **McT-1** and **McT-2**, with the increase in **$PC_{71}BM$** content, the short circuit current density (J_{sc}) increased and a corresponding increase in power conversion efficiency is obtained (shown in Table 3). This increase in photovoltaic properties with increase in fullerene content has been previously reported for oligothiophene: fullerene BHJ blends.[99,116,117] With increase in fullerene content, crystallisation of the macrocycles is prevented by the fullerenes, resulting in a BHJ morphology with enhanced mixing, favouring the exciton dissociation and photocurrent. Moreover, increased fullerene content has also been

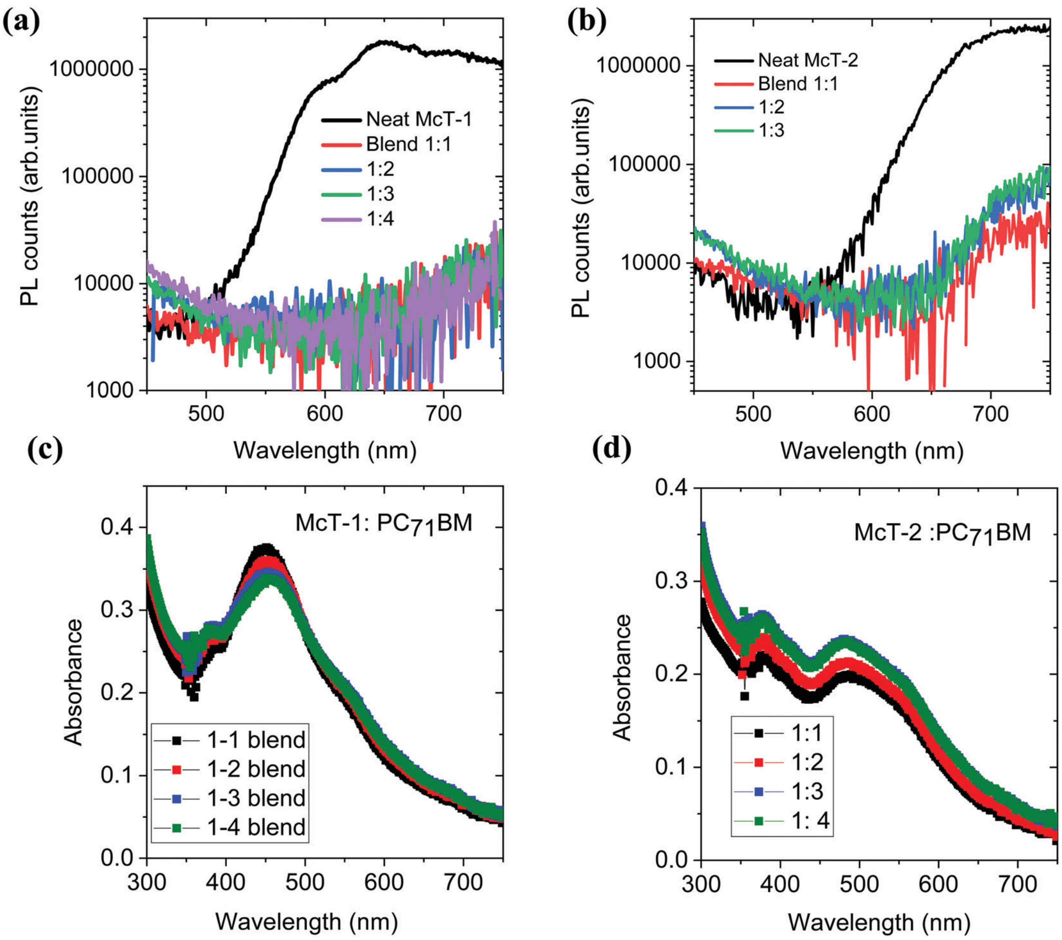

Fig. 8 Steady state photoluminescence spectra of (a) neat **McT-1** and blend with **$PC_{71}BM$** for different ratios (b) neat **McT-2** and blend with **$PC_{71}BM$** for different ratios. The excitation wavelength is 450 nm. Absorbance spectra of the (c) **McT-1** and **$PC_{71}BM$** blends (d) **McT-2** and **$PC_{71}BM$** blends as a function of different blend ratios.

Table 3 Photovoltaic performance parameters of the **McT-1**:$\mathbf{PC_{71}BM}$ and **McT-2**:$\mathbf{PC_{71}BM}$ blends for different D : A weight ratios

Blend	D : A (wt.) ratio	J_{sc} (mA cm^{-2})	V_{oc} (V)	FF (%)	R_{sh} (Ω cm^2)	R_s (Ω cm^2)	PCE avg (%)	PCE best (%)
McT-1 and $\mathbf{PC_{71}BM}$	1–1	2.84 ± 0.70	0.699 ± 0.011	33.6 ± 1.0	453 ± 31	10.3 ± 1.2	0.67 ± 0.05	0.73
	1–2	3.74 ± 0.18	0.683 ± 0.033	33.7 ± 1.7	357 ± 64	5.3 ± 1.6	0.86 ± 0.10	0.97
	1–3	3.86 ± 0.35	0.669 ± 0.019	35.3 ± 1.2	341 ± 33	3.0 ± 1.3	0.91 ± 0.11	1.05
	1–4	4.08 ± 0.29	0.662 ± 0.018	35.0 ± 0.9	303 ± 29	3.4 ± 1.3	0.95 ± 0.09	1.07
McT-2 and $\mathbf{PC_{71}BM}$	1–1	1.62 ± 0.13	0.401 ± 0.047	29.9 ± 0.3	361 ± 46	5.4 ± 1.4	0.20 ± 0.03	0.23
	1–2	2.25 ± 0.21	0.421 ± 0.038	31.4 ± 0.4	300 ± 40	2.7 ± 1.2	0.30 ± 0.04	0.34
	1–3	2.59 ± 0.26	0.682 ± 0.057	28.9 ± 1.1	392 ± 30	3.6 ± 1.5	0.51 ± 0.07	0.63
	1–4	2.62 ± 0.19	0.604 ± 0.077	29.5 ± 1.1	348 ± 39	3.1 ± 1.3	0.47 ± 0.08	0.58

reported in better percolative carrier transport pathways. However, for both donors, the main limiting factors of the photovoltaic properties are the low short circuit current density (1.6–4.0 mA cm^{-2}) and the fill factor which is below 40% even for the optimised donor:acceptor blend. One of the main contributing factors for the low J_{sc} is the narrow absorption bandwidth in the visible region. The low FF implies unfavourable nanoscale morphology of the donor:acceptor blends preventing efficient collection of photogenerated charges. For both **McT-1** and **McT-2**, under the optimised donor: acceptor blend condition, the open circuit voltage is very similar ~0.67 V. Considering the HOMO level of the **McT-1** and LUMO level of the $\mathbf{PC_{71}BM}$ as shown in Fig. 3(c), a voltage loss of less than 0.2 V is seen for the optimised blend of **McT-1:**$\mathbf{PC_{71}BM}$. **McT-2** showed in general slightly poorer V_{oc} than **McT-1** due to its higher HOMO level.

The external quantum efficiency (EQE) spectra of the **Mc-T1:** $\mathbf{PC_{71}BM}$ and **Mc-T2:**$\mathbf{PC_{71}BM}$ blends are shown in Fig. 9(c and d). For both donors, EQE increases with increase in $\mathbf{PC_{71}BM}$ content and this agrees with the increase in J_{sc} shown in Table 3. Under the optimised blend ratio of 1 : 4, **McT1:**$\mathbf{PC_{71}BM}$ shows an EQE of ~40% and for **McT1:**$\mathbf{PC_{71}BM}$, the EQE is slightly lower around 25% in the 350 to 550 nm range. Because of the narrow spectral bandwidth of the UV-Vis absorption profile and the EQE spectra of the **McT-1:**$\mathbf{PC_{71}BM}$ and **McT-2:**$\mathbf{PC_{71}BM}$, the spectral responsivity is estimated as a function of wavelength towards their use in photodetectors. The narrow spectral

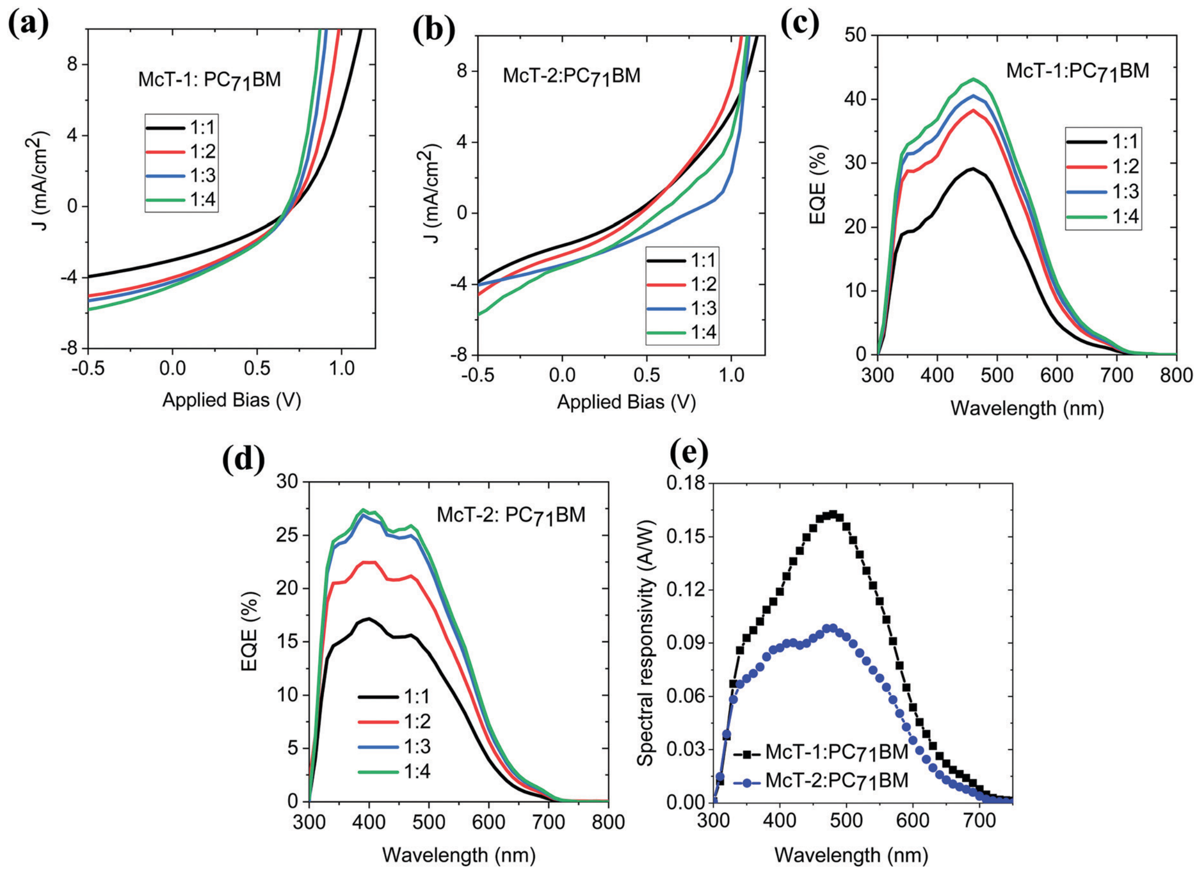

Fig. 9 *J–V* characteristics of the (a) **McT-1** : $\mathbf{PC_{71}BM}$ and (b) **McT-2** : $\mathbf{PC_{71}BM}$ blends as a function of different blend ratios. External quantum efficiency (EQE) spectra of the (c) **McT-1** : $\mathbf{PC_{71}BM}$ and (d) **McT-2** : $\mathrm{PC_{71}}$**BM** blends as a function of different blend ratios.(e) Spectral responsivity curves of the corresponding photovoltaic devices estimated from their EQE spectra.

bandwidth allows them to be used in photodetector applications without the use of filters in colour image sensing.[1,118] The corresponding spectral responsivity curves for the optimised blend ratios are shown in Fig. 9(e). For the **McT-1:PC$_{71}$BM** blend, a maximum responsivity of 0.16 A W^{-1} at 478 nm, and for **McT-2:PC$_{71}$BM**, 0.10 A W^{-1} at 478 nm are obtained under zero external bias. This zero bias responsivity values obtained are comparable to the previously reported responsivity of organic photodiodes such as **P3HT:ICBA**, **P3HT:PC$_{60}$BM** blends[119,120] and better than the recently reported responsivity of pentacene:C$_{60}$ heterostructure[121] in the blue wavelength range. This blue wavelength responsivity of **McT-1:PC$_{71}$BM** blend is relevant for the development of organic photodetectors without colour filters for imaging applications.

Conclusions

In conclusion, we show that incorporating an electron-deficient benzothiadiazole unit within a thiophene-based macrocycle red-shifts and broadens the main band of absorption while improving the absorbance in higher energy wavelengths, whereas the simplest macrocycle **McT-1** shows a higher $\varepsilon_{\max}$ value. DFT calculations indicated that the macrocycles would possess a high level of planarity with *E*,*E*-isomers being preferred, and in the case of **McT-1** this prediction was further indicated by crystallographic data. The theoretical calculations also revealed the ICT character of **McT-2**, which has a striking impact on the absorption profile. Organic field-effect transistors were fabricated, with **McT-1** exhibiting a hole mobility of 1.92×10^{-4} cm^2 V^{-1} s^{-1}. Efficient charge transfer between the macrocycles and **PC$_{71}$BM** acceptor was revealed by photoluminescence quenching studies and led us to investigate them in photovoltaic devices. For both macrocycles, the photovoltaic cells showed an increase in J_{sc} with concomitant increase of power conversion efficiency with the increase in **PC$_{71}$BM** content. The cells displayed an optimal efficiency of ~1.1% for the 1 : 4 **McT-1 : PC$_{71}$BM** blend and 0.63% 1 : 3 for the **McT-2 : PC$_{71}$BM** blend. The improvement in spectral absorption did not produce higher J_{sc} in the case of **McT-2** presumably due to unfavourable nanoscale morphology preventing efficient charge collection, as indicated by the OPV data. This is also likely due to the presence of alkyne residues, which tend to affect charge generation and OPV performance. For future studies of related macrocycles in OPVs, we encourage the total removal of alkyne residues and further investigation of the self-assembly of these molecules. In photodetectors, the **McT-1:PC$_{71}$BM** and **McT-2:PC$_{71}$BM** blends showed a maximum responsivity of 0.16 A W^{-1} at 478 nm, and 0.10 A W^{-1} at 478 nm, respectively, under zero external bias. This is a relevant result for the field of organic photodetectors without colour filters for imaging applications.

Conflicts of interest

The authors declare that they have no conflict of interest.

Acknowledgements

GC acknowledges the EPSRC for funding (EP/E036244/1). JMS acknowledges the Coordenação de Aperfeiçoamento de Pessoal de Nível Superior – Brasil (CAPES) – Finance Code 001 for PhD funding. JMS also acknowledges Dr Nor Basid Adiwibawa Prasetya for helpful advice. Dr L. K. Jagadamma acknowledges support from a Marie Skłodowska-Curie Individual Fellowship (European Commission) (MCIF: No. 745776).

References

1 D. Yang and D. Ma, Development of organic semiconductor photodetectors: From mechanism to applications, *Adv. Opt. Mater.*, 2019, **7**, 1800522.

2 G. J. Hedley, A. Ruseckas and I. D. W. Samuel, Light harvesting for organic photovoltaics, *Chem. Rev.*, 2017, **117**, 796–837.

3 Y. Liu, J. Zhao, Z. Li, C. Mu, W. Ma, H. Hu, K. Jiang, H. Lin, H. Ade and H. Yan, Aggregation and morphology control enables multiple cases of high-efficiency polymer solar cells, *Nat. Commun.*, 2014, **5**, 5293.

4 A. Bessette and G. S. Hanan, Design, synthesis and photophysical studies of dipyrromethene-based materials: Insights into their applications in organic photovoltaic devices, *Chem. Soc. Rev.*, 2014, **43**, 3342–3405.

5 Y. Cui, H. Yao, J. Zhang, T. Zhang, Y. Wang, L. Hong, K. Xian, B. Xu, S. Zhang, J. Peng, Z. Wei, F. Gao and J. Hou, Over 16% efficiency organic photovoltaic cells enabled by a chlorinated acceptor with increased open-circuit voltages, *Nat. Commun.*, 2019, **10**, 2515.

6 Z. Hassan, E. Spuling, D. M. Knoll and S. Bräse, Regioselective functionalization of [2.2] paracyclophanes: Recent synthetic progress and perspectives, *Angew. Chem., Int. Ed.*, 2020, **59**, 2156–2170.

7 M. Godumala, S. Choi, M. J. Cho and D. H. Choi, Recent breakthroughs in thermally activated delayed fluorescence organic light emitting diodes containing non-doped emitting layers, *J. Mater. Chem. C*, 2019, **7**, 2172–2198.

8 J. Roncali, Molecular engineering of the band gap of π-conjugated systems: Facing technological applications, *Macromol. Rapid Commun.*, 2007, **28**, 1761–1775.

9 L. Gonzalez, C. Liu, B. Dietrich, H. Su, S. Sproules, H. Cui, D. Honecker, D. J. Adams and E. R. Draper, Transparent-to-dark photo- and electrochromic gels, *Commun. Chem.*, 2018, **1**, 77.

10 G. Horowitz, Organic field-effect transistors, *Adv. Mater.*, 1998, **10**, 365–377.

11 F. A. Larik, F. Muhammad, A. Saeed, Q. Abbas, M. A. Kazi, N. Abbas, A. A. Thebo, D. M. Khan and P. A. Channar, Thiophene-based molecular and polymeric semiconductors for organic field effect transistors and organic thin film transistors, *J. Mater. Sci.: Mater. Electron.*, 2018, **29**, 17975–18010.

12 R. Rana, A. Jetly and R. Mehra, *An Extensive Review on Organic Light-Emitting Diode for Energy-Saving and*

Eco-friendly Technology. Applications of Computing, Automation and Wireless Systems in Electrical Engineering, Springer Singapore, 2019, DOI: 10.1007/978-981-13-6772-4_78.

13 M. S. AlSalhi, J. Alam, L. A. Dass and M. Raja, Recent advances in conjugated polymers for light emitting devices, *Int. J. Mol. Sci.*, 2011, **12**, 2036–2054.

14 M. Y. Wong and E. Zysman-Colman, Purely organic thermally activated delayed fluorescence materials for organic light-emitting diodes, *Adv. Mater.*, 2017, **29**, 1605444.

15 X. K. Chen, D. Kim and J. L. Brédas, Thermally activated delayed fluorescence (TADF) path toward efficient electroluminescence in purely organic materials: Molecular level insight, *Acc. Chem. Res.*, 2018, **51**, 2215–2224.

16 Y. Zhang, Y.-Y. Fu, D.-F. Zhu, J.-Q. Xu, Q.-G. He and J.-G. Cheng, Recent advances in fluorescence sensor for the detection of peroxide explosives, *Chin. Chem. Lett.*, 2016, **27**, 1429–1436.

17 H. Lu, Y. Zheng, X. Zhao, L. Wang, S. Ma, X. Han, B. Xu, W. Tian and H. Gao, Fluorescent probes highly efficient far red/near-infrared solid fluorophores: Aggregation-induced emission, intramolecular charge transfer, twisted molecular conformation, and bioimaging applications, *Angew. Chem., Int. Ed.*, 2016, **55**, 155–159.

18 Y. Liu, R. Bao, J. Tao, J. Li, M. Dong and C. Pan, Recent progress in tactile sensors and their applications in intelligent systems, *Sci. Bull.*, 2020, **65**, 70–88.

19 K. Shimizu, Y. Mori and S. Hotta, Laser oscillation from hexagonal crystals of a thiophene/phenylene co-oligomer, *J. Appl. Phys.*, 2014, **99**, 063505.

20 B. L. Heng, X. Wang, D. Tian, J. Zhai, B. Tang and L. Jiang, Optical waveguides based on single-crystalline organic micro-tiles, *Adv. Mater.*, 2010, **22**, 4716–4720.

21 A. J. C. Kuehne and M. C. Gather, Organic lasers: Recent developments on materials, device geometries, and fabrication techniques, *Chem. Rev.*, 2016, **116**, 12823–12864.

22 H. Li and D. Qu, Recent advances in new-type molecular switches, *Sci. China: Chem.*, 2015, **58**, 916–921.

23 J. D. Harris, M. J. Moran and I. Aprahamian, New molecular switch architectures, *Proc. Natl. Acad. Sci. U. S. A.*, 2018, **115**, 9414–9422.

24 S. Pu, Q. Sun, C. Fan, R. Wanga and G. Liua, Recent advances in diarylethene-based multi-responsive molecular switches, *J. Mater. Chem. C*, 2016, **4**, 3075–3093.

25 G. Wang, F. S. Melkonyan, A. Facchetti and T. J. Marks, All-polymer solar cells: Recent progress, challenges, and prospects, *Angew. Chem., Int. Ed.*, 2019, **58**, 4129–4142.

26 Y. Li, J. Y. Liu, Y. D. Zhao and Y. C. Cao, Recent advancements of high efficient donor–acceptor type blue small molecule applied for OLEDs, *Mater. Today*, 2017, **20**, 258–266.

27 J. Hou, O. Inganäs, R. H. Friend and F. Gao, Organic solar cells based on non-fullerene acceptors, *Nat. Mater.*, 2018, **17**, 119–128.

28 M.-A. Pan, T.-K. Lau, Y. Tang, Y.-C. Wu, T. Liu, K. Li, M.-C. Chen, X. Lu, W. Ma and C. Zhan, 16.7%-Efficiency ternary blended organic photovoltaic cells with PCBM as the acceptor additive to increase the open-circuit voltage and phase purity, *J. Mater. Chem. A*, 2019, **7**, 20713–20722.

29 T. Duan, J. Gao, T. Xu, Z. Kan, W. Chen, R. Singh, G. P. Kini, C. Zhong, D. Yu, Z. Xiao, Z. Xiao and S. Lu, Simple organic donors based on halogenated oligothiophenes for all small molecule solar cells with efficiency over 11%, *J. Mater. Chem. A*, 2020, **8**, 5843–5847.

30 H. Huang, X. Li, S. Chen, B. Qiu, J. Du, L. Meng, Z. Zhang, C. Yang and Y. Li, Enhanced performance of ternary organic solar cells with a wide bandgap acceptor as the third component, *J. Mater. Chem. A*, 2019, **7**, 27423–27431.

31 J. Yuan, Y. Zhang, L. Zhou, G. Zhang, H. L. Yip, T. K. Lau, X. Lu, C. Zhu, H. Peng, P. A. Johnson, M. Leclerc, Y. Cao, J. Ulanski, Y. Li and Y. Zou, Single-junction organic solar cell with over 15% efficiency using fused-ring acceptor with electron-deficient core, *Joule*, 2019, **3**, 1140–1151.

32 R. Haver, *et al.*, Tuning the circumference of six-porphyrin nanorings, *J. Am. Chem. Soc.*, 2019, **141**, 7965–7971.

33 M. A. Collini, M. B. Thomas, V. Bandi, P. A. Karr and F. D. Souza, Directly attached bisdonor-BF2 chelated azadipyrromethene-fullerene tetrads for promoting ground and excited state charge transfer, *Chem. – Eur. J.*, 2017, **23**, 4450–4461.

34 G. Szalóki, V. Croué, V. Carré, F. Aubriet, O. Alévêque, E. Levillain, M. Allain, J. Aragó, E. Ortí, S. Goeb and M. Sallé, Controlling the host–guest interaction mode through a redox stimulus, *Angew. Chem., Int. Ed.*, 2017, **56**, 16272–16276.

35 R. Haver and H. L. Anderson, Synthesis and properties of porphyrin nanotubes, *Helv. Chim. Acta*, 2019, **102**, 1800211.

36 W. Y. Sit, F. D. Eisner, Y. H. Lin, Y. Firdaus, A. Seitkhan, A. H. Balawi, F. Laquai, C. H. Burgess, M. A. McLachlan, G. Volonakis, F. Giustino and T. D. Anthopoulos, High-efficiency fullerene solar cells enabled by a spontaneously formed mesostructured CuSCN-nanowire heterointerface, *Adv. Sci.*, 2018, **5**, 1700980.

37 B. Zhang, M. T. Trinh, B. Fowler, M. Ball, Q. Xu, F. Ng, M. L. Steigerwald, X. Y. Zhu, C. Nuckolls and Y. Zhong, Rigid, conjugated macrocycles for high performance organic photodetectors, *J. Am. Chem. Soc.*, 2016, **138**, 16426–16431.

38 C. J. Takacs, Y. Sun, G. C. Welch, L. A. Perez, X. Liu, W. Wen, G. C. Bazan and A. J. Heeger, Solar cell efficiency, self-assembly, and dipole–dipole interactions of isomorphic narrow-band-gap molecules, *J. Am. Chem. Soc.*, 2012, **134**, 16597–16606.

39 R. B. K. Siram, K. Tandy, M. Horecha, P. Formanek, M. Stamm, S. Gevorgyan, F. C. Krebs, A. Kiriy, P. Meredith, P. L. Burn, E. B. Namdas and S. Patil, Synthesis and self-assembly of donor–acceptor–donor based oligothiophenes and their optoelectronic properties, *J. Phys. Chem. C*, 2011, **115**, 14369–14376.

40 S. Chen, Y. Wang, L. Zhang, J. Zhao, Y. Chen, D. Zhu, H. Yao, G. Zhang, W. Ma, R. H. Friend, P. C. Y. Chow, F. Gao and H. Yan, Efficient nonfullerene organic solar

cells with small driving forces for both hole and electron transfer, *Adv. Mater.*, 2018, **30**, 1804215.

41 D. Deng, Y. Yang, W. Zou, Y. Zhang, Z. Wang, Z. Wang, J. Zhang, K. Lu, W. Ma and Z. Wei, Aromatic end-capped acceptor effects on molecular stacking and the photovoltaic performance of solution-processable small molecules, *J. Mater. Chem. A*, 2018, **6**, 22077–22085.

42 Y. Firdaus, A. Seitkhan, F. Eisner, W.-Y. Sit, Z. Kan, N. Wehbe, A. H. Balawi, E. Yengel, S. Karuthedath, F. Laquai and T. D. Anthopoulos, Charge photogeneration and recombination in mesostructured CuSCN-nanowire/ $PC_{70}BM$ Solar Cells, *Sol. RRL*, 2018, **2**, 1800095.

43 M. Liu, R. Komatsu, X. Cai, K. Hotta, S. Sato, K. Liu, D. Chen, Y. Kato, H. Sasabe, S. Ohisa, Y. Suzuri, D. Yokoyama, S. J. Su and J. Kido, Horizontally orientated sticklike emitters: enhancement of intrinsic out-coupling factor and electroluminescence performance, *Chem. Mater.*, 2017, **29**, 8630–8636.

44 T. D. Schmidt, T. Lampe, M. R. Daniel Sylvinson, P. I. Djurovich, M. E. Thompson and W. Brütting, Emitter orientation as a key parameter in organic light-emitting diodes, *Phys. Rev. Appl.*, 2017, **8**, 037001.

45 S. Casalini, C. A. Bortolotti, F. Leonardi and F. Biscarini, Self-assembled monolayers in organic electronics, *Chem. Soc. Rev.*, 2017, **46**, 40–71.

46 O. V. Borshchev and S. A. Ponomarenko, Self-assembled organic semiconductors for monolayer field-effect transistors, *Polym. Sci., Ser. C*, 2014, **56**, 32–46.

47 E. Busseron, Y. Ruff, E. Moulin and N. Giuseppone, Supramolecular self-assemblies as functional nanomaterials, *Nanoscale*, 2013, **5**, 7098–7140.

48 T. Minari, C. Liu, M. Kano and K. Tsukagoshi, Controlled self-assembly of organic semiconductors for solution-based fabrication of organic field-effect transistors, *Adv. Mater.*, 2012, **24**, 299–306.

49 B. Gothe, T. De Roo, J. Will, T. Unruh, S. Mecking and M. Halik, Self-assembled monolayer field-effect transistors based on oligo-9,9′-dioctylfluorene phosphonic acids, *Nanoscale*, 2017, **9**, 18584–18589.

50 Y. Zhou, G. Long, A. Li, A. Gray-weale, Y. Chen and T. Yan, Towards predicting the power conversion efficiencies of organic solar cells from donor and acceptor molecule structures, *J. Mater. Chem. C*, 2018, **6**, 3276–3287.

51 A. O. Weldeab, A. Steen, D. L. Starkenburg, J. S. D. Williams, K. A. Abboud, J. Xue, N. I. Hammer, K. Castellano and D. L. Watkins, Tuning the structural and spectroscopic properties of donor–acceptor–donor oligomers via X-bonding, H-bonding, and π–π interactions, *J. Mater. Chem. C*, 2018, **6**, 11992–12000.

52 T. Ghosh, J. S. Panicker and V. C. Nair, Self-assembled organic materials for photovoltaic application, *Polymers*, 2017, **9**, 112.

53 S. S. Zade and M. Bendikov, Cyclic oligothiophenes: Novel organic materials and models for polythiophene. A theoretical study, *J. Org. Chem.*, 2006, **71**, 2972–2981.

54 M. Iyoda and H. Shimizu, Multifunctional π-expanded oligothiophene macrocycles, *Chem. Soc. Rev.*, 2015, **44**, 6411–6424.

55 M. Ball, B. Zhang, Y. Zhong, B. Fowler, S. Xiao, F. Ng, M. Steigerwald and C. Nuckolls, Conjugated macrocycles in organic electronics, *Acc. Chem. Res.*, 2019, **52**, 1068–1078.

56 K. Miki and K. Ohe, π-Conjugated macrocycles bearing angle-strained alkynes, *Chem. – Eur. J.*, 2020, **26**, 2529–2575.

57 M. Iyoda, Giant conjugated macrocycles: Synthesis and applications, *J. Synth. Org. Chem.*, 2012, **70**, 1157–1163.

58 M. Ball, Y. Zhong, B. Fowler, B. Zhang, P. Li, G. Etkin, D. W. Paley, J. Decatur, A. K. Dalsania, H. Li, S. Xiao, F. Ng, M. L. Steigerwald and C. Nuckolls, Macrocyclization in the design of organic n-type electronic materials, *J. Am. Chem. Soc.*, 2016, **138**, 12861–12867.

59 H. Shimizu, K. H. Park, H. Otani, S. Aoyagi, T. Nishinaga, Y. Aso, D. Kim and M. Iyoda, A Saturn-like complex composed of macrocyclic oligothiophene and C60 fullerene: Structure, stability, and photophysical properties in solution and the solid state, *Chem. – Eur. J.*, 2018, **24**, 3793–3801.

60 Y. Zhao, K. Jiang, W. Xu and D. Zhu, Macrocyclic triphenylamine based organic dyes for efficient dye-sensitized solar cells, *Tetrahedron*, 2012, **68**, 9113–9118.

61 N. Baser-kirazli, R. A. Lalancette and F. Jäkle, Enhancing the acceptor character of conjugated organoborane macrocycles: A highly electron-deficient hexaboracyclophane, *Angew. Chem.*, 2020, **59**, 8689–8697.

62 M. L. Ball, B. Zhang, T. Fu, A. M. Schattman, D. W. Paley, F. Ng, L. Venkataraman, C. Nuckolls and M. L. Steigerwald, The importance of intramolecular conductivity in three dimensional molecular solids, *Chem. Sci.*, 2019, **10**, 9339–9344.

63 K. J. Weiland, *et al.*, Mechanical stabilization of helical chirality in a macrocyclic oligothiophene, *J. Am. Chem. Soc.*, 2019, **141**, 2104–2110.

64 Y. Qin, X. Liu, P. Jia, L. Xu and H. Yang, BODIPY-Based macrocycles, *Chem. Soc. Rev.*, 2020, **49**, 5678–5703.

65 Y. Li, A. Yagi and K. Itami, Synthesis of highly twisted, nonplanar aromatic macrocycles enabled by an axially chiral 4,5-diphenylphenanthrene building block, *J. Am. Chem. Soc.*, 2020, **142**, 3246–3253.

66 M. A. Sabuj, M. M. Huda and N. Rai, Donor–acceptor conjugated macrocycles with polyradical character and global aromaticity, *iScience*, 2020, **23**, 101675.

67 T. Zhao, Z. Liu, Y. Song, W. Xu, D. Zhang and R. V. June, Novel diethynylcarbazole macrocycles: Synthesis and optoelectronic properties, *J. Org. Chem.*, 2006, **71**, 7422–7432.

68 J. D. Cojal González, M. Iyoda and J. P. Rabe, Templated bilayer self-assembly of fully conjugated π-expanded macrocyclic oligothiophenes complexed with fullerenes, *Nat. Commun.*, 2017, **8**, 14717.

69 S. Nishigaki, M. Fukui, H. Sugiyama, H. Uekusa, S. Kawauchi, Y. Shibata and K. Tanaka, Synthesis, structures, and photophysical properties of alternating donor–acceptor cycloparaphenylenes, *Chem. – Eur. J.*, 2017, **23**, 7227–7231.

70 H. Ito, Y. Mitamura, Y. Segawa and K. Itami, Thiophene-based, radial π-conjugation: Synthesis, Structure, and

photophysical properties of cyclo-1,4-phenylene-2′,5′-thienylenes, *Angew. Chem.*, 2015, **54**, 159–163.

71 M. Iyoda, J. Yamakawa and M. J. Rahman, Conjugated macrocycles: Concepts and applications, *Angew. Chem.*, 2011, **50**, 10522–10553.

72 F. Zhang, G. Götz, H. D. F. Winkler, C. A. Schalley and P. Bäuerle, Giant cyclo[*n*]thiophenes with extended π conjugation, *Angew. Chem.*, 2009, **48**, 6632–6635.

73 S. V. Mulay, O. Dishi, Y. Fang, M. R. Niazi, L. J. W. Shimon, D. F. Perepichkab and O. Gidron, A macrocyclic oligofuran: Synthesis, solid state structure and electronic properties, *Chem. Sci.*, 2019, **10**, 8527–8532.

74 K. Nakao, M. Nishimura, T. Tamachi, Y. Kuwatani, H. Miyasaka, T. Nishinaga and M. Iyoda, Giant macrocycles composed of thiophene, acetylene, and ethylene building blocks, *J. Am. Chem. Soc.*, 2006, **128**, 16740–16747.

75 M. Iyoda, Giant macrocycles composed of thiophene, acetylene, and ethylene units, *C. R. Chim.*, 2009, **12**, 395–402.

76 H. Shimizu, J. D. Cojal González, M. Hasegawa, T. Nishinaga, T. Haque, M. Takase, H. Otani, J. P. Rabe and M. Iyoda, Synthesis, structures, and photophysical properties of π-expanded oligothiophene 8-mers and their saturn-like C_{60} complexes, *J. Am. Chem. Soc.*, 2015, **137**, 3877–3885.

77 M. Iyoda, H. Shimizu, S. Aoyagi, H. Okada, B. Zhou and Y. Matsuo, Structures and properties of Saturn-like complexes composed of oligothiophene macrocycle with methano[60]fullerene and [70]fullerene, *Can. J. Chem.*, 2017, **319**, 315–319.

78 J. M. Macleod, O. Ivasenko, C. Fu, T. Taerum, F. Rosei and D. F. Perepichka, Supramolecular ordering in oligothiophene-fullerene monolayers, *J. Am. Chem. Soc.*, 2009, **131**, 16844–16850.

79 R. Inoue, M. Hasegawa, T. Nishinaga, K. Yoza and Y. Mazaki, Efficient synthesis, structure, and complexation studies of electron-donating thiacalix[*n*]dithienothiophene, *Angew. Chem., Int. Ed.*, 2015, **54**, 2734–2738.

80 S. Gao, Z. Yang, Y. Wang, G. Zhang and Y. Hu, Spin-polarized transport and optoelectronic properties of a novel-designed architecture with a porphyrin-based wheel and organometallic multidecker sandwich complex-based axle, *JOM*, 2020, **72**, 3149–3159.

81 Y. Xu, S. Gsänger, M. B. Minameyer, I. Imaz, D. Maspoch, O. Shyshov, F. Schwer, X. Ribas, T. Drewello, B. Meyer and M. von Delius, Highly strained, radially π-conjugated porphyrinylene nanohoops, *J. Am. Chem. Soc.*, 2019, **141**, 18500–18507.

82 S. Izumi, A. Nyga, P. de Silva, N. Tohnai, S. Minakata, P. Data and Y. Takeda, Revealing topological influence of phenylenediamine unit on physicochemical properties of donor–acceptor–donor–acceptor thermally activated delayed fluorescent macrocycles, *Chem. – Asian J.*, 2020, **15**, 4098–4103.

83 Z. He, X. Xu, X. Zheng, T. Ming and Q. Miao, Conjugated Macrocycles of phenanthrene: A new segment of [6,6]-carbon nanotube and solution-processed organic semiconductors, *Chem. Sci.*, 2013, **4**, 4525–4531.

84 K. Singh, T. S. Virk, J. Zhang, W. Xu and D. Zhu, Neutral tetrathia[22]annulene[2.1.2.1] based field-effect transistors: Improved on/off ratio defies ring puckering, *Chem. Commun.*, 2012, **48**, 12174–12176.

85 W. Zhao, *et al.*, Transistors from a conjugated macrocycle molecule: Field and photo effects, *Chem. Commun.*, 2008, 4324–4326.

86 S. Q. Zhang, Z. Y. Liu, W. F. Fu, F. Liu, C. M. Wang, C. Q. Sheng, Y. F. Wang, K. Deng, Q. D. Zeng, L. J. Shu, J. H. Wan, H. Z. Chen and T. P. Russell, Donor–acceptor conjugated macrocycles: Synthesis and host–guest coassembly with fullerene toward photovoltaic application, *ACS Nano*, 2017, **11**, 11701–11713.

87 S. Izumi, H. F. Higginbotham, A. Nyga, P. Stachelek, N. Tohnai, P. De Silva, P. Data, Y. Takeda and S. Minakata, Thermally activated delayed fluorescent donor–acceptor–donor–acceptor π-conjugated macrocycle for organic light-emitting diodes, *J. Am. Chem. Soc.*, 2020, **142**, 1482–1491.

88 M. L. Ball, B. Zhang, Q. Xu, D. W. Paley, V. C. Ritter, F. Ng, M. L. Steigerwald and C. Nuckolls, Influence of molecular conformation on electron transport in giant, conjugated macrocycles, *J. Am. Chem. Soc.*, 2018, **140**, 10135–10139.

89 C. Li, C. Wang, Y. Guo, Y. Jin, N. Yao, Y. Wu, F. Zhang and W. Li, A diketopyrrolopyrrole-based macrocyclic conjugated molecule for organic electronics, *J. Mater. Chem. C*, 2019, **7**, 3802–3810.

90 J. Zhu, W. Song, T. Zhang, Q. Dong, J. Huang, H. Zhou and J. Su, Tetrabenzeneaza macrocycle: A novel platform for universal high-performance hole transport materials, *Dyes Pigm.*, 2021, **186**, 108981.

91 M. Bourass, A. Touimi Benjelloun, M. Benzakour, M. McHarfi, F. Jhilal, M. Hamidi and M. Bouachrine, The optoelectronic properties of organic materials based on triphenylamine that are relevant to organic solar photovoltaic cells, *New J. Chem.*, 2017, **41**, 13336–13346.

92 Y.-J. Cheng, S.-H. Yang and C.-S. Hsu, Synthesis of conjugated polymers for organic solar cell applications, *Chem. Rev.*, 2009, **109**, 5868–5923.

93 M. T. Dang, L. Hirsch and G. Wantz, P3HT:PCBM, best seller in polymer photovoltaic research, *Adv. Mater.*, 2011, **23**, 3597–3602.

94 S. Holliday, R. S. Ashraf, A. Wadsworth, D. Baran, S. A. Yousaf, C. B. Nielsen, C. Tan, S. D. Dimitrov, Z. Shang, N. Gasparini, M. Alamoudi, F. Laquai, C. J. Brabec, A. Salleo, J. R. Durrant and I. Mcculloch, High-efficiency and air-stable P3HT-based polymer solar cells with a new non-fullerene acceptor, *Nat. Commun.*, 2016, **7**, 11585.

95 S. H. Liao, H. J. Jhuo, Y. S. Cheng and S. A. Chen, Fullerene derivative-doped zinc oxide nanofilm as the cathode of inverted polymer solar cells with low-bandgap polymer (PTB7-Th) for high performance, *Adv. Mater.*, 2013, **25**, 4766–4771.

96 B. Kan, M. Li, Q. Zhang, F. Liu, X. Wan, Y. Wang, W. Ni, G. Long, X. Yang, H. Feng, Y. Zuo, M. Zhang, F. Huang, Y. Cao, T. P. Russell and Y. Chen, A series of simple oligomer-like small molecules based on oligothiophenes for solution-processed solar cells with high efficiency, *J. Am. Chem. Soc.*, 2015, **137**, 3886–3893.

97 Y. Wang, H. Guo, A. Harbuzaru, M. A. Uddin, I. Arrechea-Marcos, S. Ling, J. Yu, Y. Tang, H. Sun, J. T. López Navarrete, R. P. Ortiz, H. Y. Woo and X. Guo, (Semi)ladder-type bithiophene imide-based all-acceptor semiconductors: Synthesis, structure–property correlations, and unipolar n-type transistor performance, *J. Am. Chem. Soc.*, 2018, **140**, 6095–6108.

98 C. Zhang and X. Zhu, Thieno[3,4-*b*]thiophene-based novel small-molecule optoelectronic materials, *Acc. Chem. Res.*, 2017, **50**, 1342–1350.

99 Y. Lin, Y. Li and X. Zhan, Small molecule semiconductors for high-efficiency organic photovoltaics, *Chem. Soc. Rev.*, 2012, **41**, 4245–4272.

100 P. Kumaresan, S. Vegiraju, Y. Ezhumalai, S. L. Yau, C. Kim, W. H. Lee and M. C. Chen, Fused-thiophene based materials for organic photovoltaics and dye-sensitized solar cells, *Polymers*, 2014, **6**, 2645–2669.

101 Y. Wang, Q. Liao, G. Wang, H. Guo, X. Zhang, M. A. Uddin, S. Shi, H. Su, J. Dai, X. Cheng, A. Facchetti, T. J. Marks and X. Guo, Alkynyl-functionalized head-to-head linkage containing bithiophene as a weak donor unit for high-performance polymer semiconductors, *Chem. Mater.*, 2017, **29**, 4109–4121.

102 J. Marques dos Santos, M. Neophytou, A. Wiles, C. T. Howells, R. S. Ashraf, I. McCulloch and G. Cooke, Influence of alkyne spacers on the performance of thiophene-based donors in bulk-heterojunction organic photovoltaic cells, *Dyes Pigm.*, 2021, **188**, 109152.

103 M. Williams-harry, A. Bhaskar, G. Ramakrishna, T. Goodson, M. Imamura, A. Mawatari, K. Nakao, H. Enozawa, T. Nishinaga and M. Iyoda, Giant thienylene-acetylene-ethylene macrocycles with large two-photon absorption cross section and semishape-persistence, *J. Am. Chem. Soc.*, 2008, **130**, 3252–3253.

104 M. Iyoda, K. Tanaka, H. Shimizu, M. Hasegawa, T. Nishinaga, T. Nishiuchi, Y. Kunugi, T. Ishida, H. Otani, H. Sato, K. Inukai, K. Tahara and Y. Tobe, Multifunctional π-expanded macrocyclic oligothiophene 6-mers and related macrocyclic oligomers, *J. Am. Chem. Soc.*, 2014, **136**, 2389–2396.

105 M. Li, H. Zhang, Y. Zhang, B. Hou, C. Li, X. Wang, J. Zhang, L. Xiao, Z. Cui and Y. Ao, Facile synthesis of benzothiadiazole-based chromophores for enhanced performance of second-order nonlinear optical materials, *J. Mater. Chem. C*, 2016, **4**, 9094–9102.

106 K. Ma, Y. Zhao, X. Han, J. Ding, X. Meng and H. Hou, Interesting pH-responsive behavior in benzothiadiazole-derived coordination polymer constructed *via* an in situ click synthesis, *Cryst. Growth Des.*, 2018, **18**, 7419–7425.

107 B. Behramand, F. Molin and H. Gallardo, 2,1,3-Benzoxadiazole and 2,1,3-benzothiadiazole-based fluorescent compounds: Synthesis, characterization and photophysical/electrochemical properties, *Dyes Pigm.*, 2012, **95**, 600–605.

108 H. Ma, C. Zhao, H. Meng, R. Li, L. Mao, D. Hu, M. Tian, J. Yuan and Y. Wei, Multifunctional organic fluorescent probe with aggregation-induced emission characteristics: Ultrafast tumor monitoring, two-photon imaging, and image-guide photodynamic therapy, *ACS Appl. Mater. Interfaces*, 2021, **13**, 7987–7996.

109 T. C. Lovell, Z. R. Garrison and R. Jasti, Synthesis, characterization, and computational investigation of bright orange-emitting benzothiadiazole [10]cycloparaphenylene, *Angew. Chem., Int. Ed.*, 2020, **59**, 14363–14367.

110 L. K. Jagadamma, L. J. McCarron, A. A. Wiles, V. Savikhin, M. T. Sajjad, M. Yazdani, V. M. Rotello, M. F. Toney, G. Cooke and I. D. W. Samuel, Triptycene as a supramolecular additive in PTB7:PCBM blends and its influence on photovoltaic properties, *ACS Appl. Mater. Interfaces*, 2018, **10**, 24665–24678.

111 S. Mondal, S. Chakraborty, S. Bhowmick and N. Das, Synthesis of triptycene-based organosoluble, thermally stable, and fluorescent polymers: Efficient host-guest complexation with fullerene, *Macromolecules*, 2013, **46**, 6824–6831.

112 G. Liu, C. Weng, P. Yin, S. Tan and P. Shen, Impact of the number of fluorine atoms on crystalline, physicochemical and photovoltaic properties of low bandgap copolymers based on 1,4-dithienylphenylene and diketopyrrolopyrrole, *Polymer*, 2017, **125**, 217–226.

113 P. Yin, T. Zheng, Y. Wu, G. Liu, Z. G. Zhang, C. Cui, Y. Li and P. Shen, Achieving efficient thick active layer and large area ternary polymer solar cells by incorporating a new fused heptacyclic non-fullerene acceptor, *J. Mater. Chem. A*, 2018, **6**, 20313–20326.

114 C. M. Cardona, W. Li, A. E. Kaifer, D. Stockdale and G. C. Bazan, Electrochemical considerations for determining absolute frontier orbital energy levels of conjugated polymers for solar cell applications, *Adv. Mater.*, 2011, **23**, 2367–2371.

115 T. Matsuno, M. Someya, S. Sato, S. Maeda and H. Isobe, Ineffective OH pinning of the flipping dynamics of a spherical guest within a tight-fitting tube, *Angew. Chem.*, 2020, **132**, 14678–14684.

116 C. R. Lomas and J. M. Hodgkiss, Templated growth of fullerene C60 crystals by triptycene in polymer blend films, *Supramol. Chem.*, 2012, **24**, 526–531.

117 J. Marques dos Santos, L. K. Jagadamma, N. M. Latif, A. Ruseckas, I. D. W. Samuel and G. Cooke, BODIPY derivatives with near infra-red absorption as small molecule donors for bulk heterojunction solar cells, *RSC Adv.*, 2019, **9**, 15410–15423.

118 J. Pan, W. Deng, X. Xu, T. Jiang, X. Zhang and J. Jie, Photodetectors based on small-molecule organic semiconductor crystals, *Chin. Phys. B*, 2019, **28**, 38102.

119 R. D. J. Vuuren, A. Armin, A. K. Pandey, P. L. Burn and P. Meredith, Organic photodiodes: The future of full color detection and image sensing, *Adv. Mater.*, 2016, **28**, 4766–4802.

120 C. Fuentes-hernandez, W. Chou, T. M. Khan, L. Diniz, J. Lukens, F. A. Larrain, V. A. Rodriguez-toro and B. Kippelen, Large-area low-noise flexible organic photodiodes for detecting faint visible light, *Science*, 2020, **370**, 698–701.

121 D. Nath, P. Dey, A. M. Joseph, J. K. Rakshit and J. N. Roy, Zero bias high responsive visible organic photodetector based on pentacene and C60, *Opt. Laser Technol.*, 2020, **131**, 106393.